Discovery of non-equilibrium ionization plasma associated with the North Polar Spur and Loop I

Marino Yamamoto,[1][*] Jun Kataoka,[1] Yoshiaki Sofue[2]

[1]*Faculty of Science and Engineering, Waseda University, 3-4-1, Okubo, Shinjuku, Tokyo 169-8555, Japan*
[2]*Institute of Astronomy, The University of Tokyo, 2-21-2, Osawa, Mitaka-shi, Tokyo 181-0015, Japan*

ABSTRACT

We investigated the detailed plasma condition of the North Polar Spur (NPS)/Loop I using archival *Suzaku* data. In previous research collisional ionization equilibrium (CIE) have been assumed for X-ray plasma state, but we also assume non-equilibrium ionization (NEI) to check the plasma condition in more detail. We found that most of the plasma in the NPS/Loop I favors the state of NEI, and has the density-weighted ionization timescale of $n_e t \sim 10^{11-12}$ s cm^{-3} and the electron number density $n_e \sim$ a few $\times 10^{-3}$ cm^{-3}. The plasma shock age, t, or the time elapsed after the shock front passed through the plasma, is estimated to be on the order of a few Myr for the NPS/Loop I, which puts a strict lower limit to the age of the whole NPS/Loop I structure. We found that NEI results in significantly higher temperature and lower emission measure than those currently derived under CIE assumption. The electron temperature under NEI is estimated to be as high as 0.5 keV toward the brightest X-ray NPS ridge at $\Delta\theta = -20°$, which decreases to 0.3 keV at $-10°$, and again increases to ~ 0.6 keV towards the outer edge of Loop I at $\Delta\theta \sim 0°$, about twice the currently estimated temperatures. Here, $\Delta\theta$ is the angular distance from the outer edge of Loop I. We discuss the implication of introducing NEI for the research in plasma states in astrophysical phenomena.

Key words: Galaxy: halo - X-rays: ISM - ISM: bubbles - Galaxy: evolution

1 INTRODUCTION

Large structures in the direction of the Galactic Center (GC) have been discovered by observations at various wavelengths. An excess of microwaves, called *WMAP* haze (Finkbeiner 2004), has been identified by *WMAP*, and this has also been confirmed by *Planck* observations (Planck Collaboration et al. 2013). Numerous Galactic spurs and loops have been observed by radio continuum surveys (e.g., Berkhuijsen et al. (1971); Haslam et al. (1982)), and more recently by *WMAP* (Vidal et al. 2015), of which Loop I is the largest structure, spanning $\sim 120°$ on the sky. Similarly, in X-rays, Loop I has been confirmed by the *ROSAT* all-sky survey (RASS) at 0.75 keV (Snowden et al. 1995), and a particularly bright structure in its northeastern part is called the North Polar Spur (NPS). Although RASS did not find corresponding features in the southern part of the GC, an all-sky survey of *eROSITA* launched in 2019 (Predehl et al. 2021) discovered relatively weak, but giant bubble-like structures, *eROSITA* bubbles, with a north-south symmetry and extending over $80°$ against the GC. γ-ray observations by the Large Area Telescope (LAT; Atwood et al. (2009)) on *Fermi* have also revealed the existence of bubbles structure extending $50°$ above and below the GC, which is called the Fermi bubble (Su et al. 2010). It has been argued that the symmetric north-south bubbles observed by *Fermi* and *eROSITA* may be a remnant of the GC explosion in the past (Sofue 2000; Sofue & Kataoka 2021).

It is still debated whether NPS/Loop I is a nearby ($100-200$ pc)

structure associated with recent supernova remnants (SNRs) or a distant structure formed by the outflow from the GC over several Myr ago. When NPS/Loop I was first discovered, the prevailing theory was that it is a nearby SNR in the vicinity of the Sun because of its north-south asymmetry. Moreover, the visual alignment of the stellar/dust polarization with the synchrotron emission in the radio band also supports this idea (Bingham 1967; Berkhuijsen et al. 1971; Egger & Aschenbach 1995). After the discovery of the Fermi bubbles, however, the competing idea that it is a remnant of the GC explosion (Sofue 1977, 2000; Bland-Hawthorn & Cohen 2003) has come into the spotlight. The X-ray emission from NPS/Loop I is well represented by a thin thermal emission at $kT \simeq 0.3$ keV under the process of ionization equilibrium by *Suzaku* and other observations (Kataoka et al. 2013; Akita et al. 2018; LaRocca et al. 2020; Kataoka et al. 2021). This is slightly higher than the typical Galactic halo (GH) temperature of 0.2 keV (Yoshino et al. 2009); thus it can be interpreted as shock-heated GH gas. In this context, the shock velocity after the GC explosion was estimated as $v_{sh} \sim 300$ km s^{-1}, with the total energy released being 10^{55-56} erg and the explosion occurring over 10 Myr ago (Kataoka et al. 2018). Nevertheless, the distance to NPS/Loop I is still debated based on the most recent measurements of radio polarization and the X-ray absorption measurements due to the interstellar medium (ISM) (Sofue 2015; Panopoulou et al. 2021).

In either formation scenario, whether due to the GC explosion or a nearby SNR, the material ejected by the explosion collides with the surrounding ISM to form a collisionless shock wave. In the case of a young SNR, it is generally observed that the plasma is in a state of non-equilibrium ionization (NEI) (Willingale et al. 2002; Bamba et al. 2003), where the ionization temperature T_z is not equal to

either the temperature of the electrons (T_e) or that of protons (T_p). Such a state of non-equilibrium develops when the heating of the plasma occurs in a very short timescale compared to the relaxation time. The degree of ionization of the plasma at t is characterized by a density-weighted timescale $n_e t$, which is expressed as a product of electron density n_e and shock age t, where $n_e t \sim 10^{12} \mathrm{s\,cm^{-3}}$ is required to reach an equilibrium for the plasma (Smith & Hughes 2010). Note that if the electron density, n_e is measured from the emission measure of the observed X-ray spectrum, then the age of the SNR plasma since it was heated, t which is called shock age, can be estimated from the above density-weighted timescale. Note that shock age is the time since the plasma was heated by the shock wave, where density-weighted timescale $n_e t = 0$ in front of the shock wave ($t = 0$) (Borkowski et al. 2001). Similarly, a timescale in which the NPS/Loop I plasma is heated may be estimated from $n_e t$ of the X-ray emitting plasma. However, all previous studies have assumed that plasma in the NPS/Loop I is in CIE, but such an assumption may not hold, particularly in low-density ($n_e \ll 1 \mathrm{cm^{-3}}$) plasma such as the GH gas.

In this study, we revisited the archival data of the *Suzaku* X-ray Imaging Spectrometer (XIS : Koyama et al. (2007)) to examine the degree of ionization equilibrium in the NPS/Loop I region to estimate their origin. The remainder of this paper is organized as follows: Section 2 describes the analysis region and criteria for data reduction when preparing the data to be used for the analysis. In Section 3, we describe the analysis method used to extract the spectra of X-ray diffuse emission and its analysis results. We discuss the physical origin of the NPS/Loop I by summarizing the results obtained from the analysis in Section 4. We also discuss future prospects. All statistical errors in the text and tables are 1σ, unless otherwise stated.

2 OBSERVATION AND DATA REDUCTION

2.1 Archival Data and Analysis Region

We used the *Suzaku* XIS archive of X-ray data for our analysis. The *Suzaku* satellite (Mitsuda et al. 2007) is equipped with four focal-plane X-ray CCD cameras (XIS), a X-ray microcalorimeter (XRS : Kelley et al. (2007)) at the focal points of five reflectors, XRT, and a non-imaging hard X-ray detector (HXD : Takahashi et al. (2007)) that measures observations above 10 keV. Among the four XISs, XIS0, 2 and 3 are front-illuminated (FI) and XIS1 is back-illuminated (BI), covering the energy range of $0.2-12$ keV. However, XIS2 was damaged in November 2006 due to contamination by a leaked charge; therefore, data from the other three XISs were used in this analysis. We did not analyze the HXD data because the anticipated emissions from the NPS in this band are too weak compared to both the instrumental and cosmic X-ray background (CXB) (Kataoka et al. 2013). The *Suzaku* is particularly suitable for studying diffuse emission, as relevant for this work, because of its high energy resolution at low energies and its low background.

In this analysis, we used the region of bright emission in RASS as measured in the 0.75 keV (R34) band around the northern bubble, such as the NPS/Loop I structure. For the low-latitude NPS/loop I region ($b < 50°$), we used data from the brightest region (Miller et al. 2008) and the eight pointing regions across the edge of the northeast bubble were observed as part of the AO7 program (Kataoka et al. 2013). In addition, in the high-latitude NPS/Loop I ($b > 50°$), the regions analyzed in a previous study (Akita et al. 2018) were selected for analysis. The regions and information used in this analysis are shown in Figure 1 and Table 2.

2.2 Data Reduction of XIS

To reduce and analyze the *Suzaku* data, we used HEASOFT version 6.27, XSPEC version 12.11.0, XRONOS version 6.0, and calibration database (CALDB) released on October 10, 2018. We followed the processes described in 'The Suzaku Data Reduction Guide' [1]. First, XSELECT was used to combine the data of different observation modes (3×3, 5×5) to the cleaned events that have already been screened for XIS 0, 1, and 3. These criteria were used to perform data reduction based on the mkf file using XSELECT : (1) data during and up to 436 s after the South Atlantic Anomaly (SAA) are not used ; (2) data above 5° and 20° from the rim of the earth (ELV) at night and daytime, respectively ; (3) we selected data with a cutoff rigidity (COR) higher than 6 GeV ; and (4) remove data when the satellite is turned off by more than 1.5 arcmin from the mean pointing angle to eliminate misalignment of the satellite's attitude after the maneuver. Furthermore, calibration sources, hot pixels, and flickering pixels were excluded based on the information regarding the status of each event.

Solar wind charge exchange (SWCX) can cause contamination of the O_{VII} emission line contamination near 0.525 keV. Since SWCX is correlated with the proton flux in the solar wind, we did not use the data taken when the solar wind flux was above $4.0 \times 10^8 \mathrm{cm^{-2}s^{-1}}$ (Yoshino et al. 2009). In addition, we checked the light curve around 0.5 keV and no flares occurred during the time of use. The proton flux was from OMNIWEB[2]. The ELV of the day-earth was set to more than 40° in the ON 11 region because the O_{VII} emission could not be sufficiently removed.

2.3 Extracting Spectra

Before extracting the spectra, we created images of XIS 0, 1 and 3 in $0.4-10$ keV. When generating images, count rate correction was performed with XISEXPMAPGEN (Ishisaki et al. 2007) and non-X-ray background (NXB) estimated from the night Earth observation data was removed with XISNXBGEN (Tawa et al. 2008). These images were also corrected for vignetting using XISSIM (Ishisaki et al. 2007).

XIMAGE was used to detect point sources in the field of view with a significance of at least 3σ for the combined XIS0 and XIS3 images in order to improve the statics. For the analysis of diffuse emissions, we created and used a region file that excludes regions with a radius of more than 2 arcmin, centered on the coordinates of the detected source in the field of view. For the regions that excluded point sources, we then created spectra of all events and NXB spectra using XISNXBGEN. We also created redistribution matrix files (RMFs) and auxillary response files (ARFs) using xisrmfgen and xissimarfgen (Ishisaki et al. 2007). ARFs were created assuming uniform radiation from a circle of radius 20 arcmin.

3 RESULTS

3.1 Spectral Analysis

We fit the spectra using XSPEC, with the energy channels chosen so that each bin contained at least 20 photons. The energy range used is $0.6-7.0$ keV for XIS0 and 3, and $0.4-5.0$ keV for XIS1 due to its sensitivity at low energy and high background at high energy

---

[1] https://heasarc.gsfc.nasa.gov/docs/suzaku/analysis/abc/
[2] https://omniweb.gsfc.nasa.gov/form/dx1.html

Table 1. *Suzaku* observation

Name	Obs ID	Start Time	Stop Time (UT)	R.A. (deg) [a]	Decl. (deg) [b]	l (deg) [c]	b (deg) [d]	Exposure (ks) [e]
			low-latitude NPS/Loop I region ($b < 50°$)					
N1	507006010	2012 Aug 8 10:23	2012 Aug 8 23:03	233.401	9.076	15.480	47.714	19.2
N2	507005010	2012 Aug 7 23:41	2012 Aug 8 10:22	233.623	8.079	14.388	47.011	15.1
N3	507004010	2012 Aug 7 10:31	2012 Aug 7 23:40	233.834	7.087	13.321	46.308	19.3
N4	507003010	2012 Aug 6 23:20	2012 Aug 7 10:30	234.034	6.098	12.280	45.606	18.1
N5	507001010	2012 Aug 5 23:04	2012 Aug 6 09:33	234.250	5.090	11.255	44.871	16.4
N6	507002010	2012 Aug 6 09:34	2012 Aug 6 23:18	234.405	4.131	10.263	44.204	20.9
N7	507007010	2012 Aug 8 23:06	2012 Aug 9 10:20	234.551	3.174	9.291	43.537	18.0
N8	507008010	2012 Aug 9 10:21	2012 Aug 9 23:53	234.713	2.200	8.334	42.838	20.9
NPS	100038010	2005 Oct 3 11:29	2005 Oct 4 10:50	260.588	4.757	26.840	21.960	39.5
			high-latitude NPS/Loop I region ($b > 50°$)					
ON-8	802038010	2007 Jul 14 17:09	2007 Jul 15 13:50	225.629	8.293	7.819	53.735	28.2
ON-9	805041010	2011 Jan 14 11:37	2011 Jan 17 04:34	192.151	−5.791	301.636	57.074	76.2
ON-10	802039010	2007 Jun 17 20:11	2007 Jun 18 22:10	192.513	5.456	301.998	68.325	33.4
ON-11	509062010	2014 Dec 20 00:12	2014 Dec 20 12:36	200.607	7.382	324.764	68.930	13.8
ON-12	509059010	2014 Dec 23 18:49	2014 Dec 24 05:16	201.171	8.665	327.544	69.932	18.3
ON-13	702053010	2008 Jan 7 07:23	2008 Jan 8 16:19	206.913	12.350	347.389	70.203	42.6
ON-14	804048010	2010 Jan 23 01:08	2010 Jan 24 14:00	202.357	11.020	333.767	71.580	42.0
ON-15	701080010	2006 Jun 18 05:29	2006 Jun 19 05:04	197.244	11.578	318.614	73.913	28.5
ON-16	805074010	2010 Dec 17 19:04	2010 Dec 18 00:57	201.743	13.573	336.170	74.105	12.3
OFF-4	702067010	2007 Jul 14 08:31	2007 Jul 14 17:00	204.195	−0.819	326.078	59.999	12.0
OFF-7	705011010	2011 Jan 17 04:38	2011 Jan 17 17:54	198.188	0.850	314.829	63.228	39.5

Note - The names N1-N8 refer to Kataoka et al. (2013), NPS to Miller et al. (2008), and Loop I ON and OFF to the region analyzed in Akita et al. (2018).
[a] R.A. (Right ascension) of *Suzaku* pointing center in J2000 equinox.
[b] Decl. (Declination) of *Suzaku* pointing center in J2000 equinox.
[c] Galactic longitude of *Suzaku* pointing center.
[d] Galactic latitude of *Suzaku* pointing center.
[e] Exposure time of a good time interval after the data reduction described in Section 2.

because of BI. An example (N8 region) of the spectrum analysis result is shown in Figure 2.

Following previous works, the X-ray diffuse emission has been modeled by a combination of three emission components (Yoshino et al. 2009; Kataoka et al. 2013); (1) unabsorbed thermal emission from local hot bubbles (LHB) and/or SWCX at a fixed $kT = 0.1$ keV and $Z = Z_⊙$, (2) absorbed thermal emission related to the GH and NPS/Loop I at a fixed $Z = 0.2Z_⊙$, and (3) absorbed cosmic X-ray background (CXB). The neutral absorption column density $N_{H,Gal}$ is fixed at the full Galactic column value [3] (Dickey & Lockman 1990). LHB/SWCX is represented `apec`, which is the model of CIE, and CXB is expressed by a power law with the photon index fixed at $Γ = 1.41$, as determined by Kushino et al. (2002). The normalization of all components tied between instruments was set to free.

In addition, the contribution of unabsorbed thermal plasma with $kT ∼ 0.1$ keV is proposed to account for low-energy spectra below 0.5 keV (Miller et al. 2008; LaRocca et al. 2020). Therefore, we also performed the analysis by adding an absorbed $kT ∼ 0.1$ keV thermal plasma. The results showed that the parameters for (2), namely, temperature, EM, and the density weighted timescale of the GH and NPS/Loop I components, are unchanged within the error range (see, Appendix for an example case of the spectral fitting of N8). Moreover, statistical improvement is negligible in most cases; a part of the reason may be due to the relatively low photon statistics of *Suzaku* XIS below 0.5 keV. Therefre, in this paper, we thus followed the

three-component model initially proposed by Kataoka et al. (2013), and subsequent papers.

Especially important for this analysis is that we utilized two different models to represent the thermal plasma emission of the GH component: `apec` and `nei`, which correspond to the CIE and NEI, respectively. The fitting results for the GH component are presented in the Table 2. Note that the emission measure (EM) is calculated from Eq. (1) of the Stawarz et al. (2013) by considering the ARF and assuming a circular radiation region of 20 arcmin.

3.2 Spatial variation of kT, EM and $n_e t$

Figure 3 shows the variation of kT, EM, and density-weighted timescale determined from the analysis as measured in the regions in NPS/Loop I. Note that the horizontal axis shows the separation angle from the outer edge of the NPS/Loop I structure defined by the coordinate in Table 3 and the magenta dashed line in Fig. 1. These coordinates of the outer edge of this NPS/Loop I are defined to be consistent with the eRosita bubble observed by the allsky survey of eRosita (Predehl et al. 2020). The angle increases from the outer to the inner parts of the northern bubble; thus, the GC direction corresponds to a positive value. Furthermore, the temperature estimated in this fitting is the electron temperature, which will be denoted as kT in this paper.

For all regions, the EM of the GH component was larger in the `apec` model than in the `nei` model. Focusing on the continuous observation of low-latitude NPS/Loop I region (N1-N8) in particular,

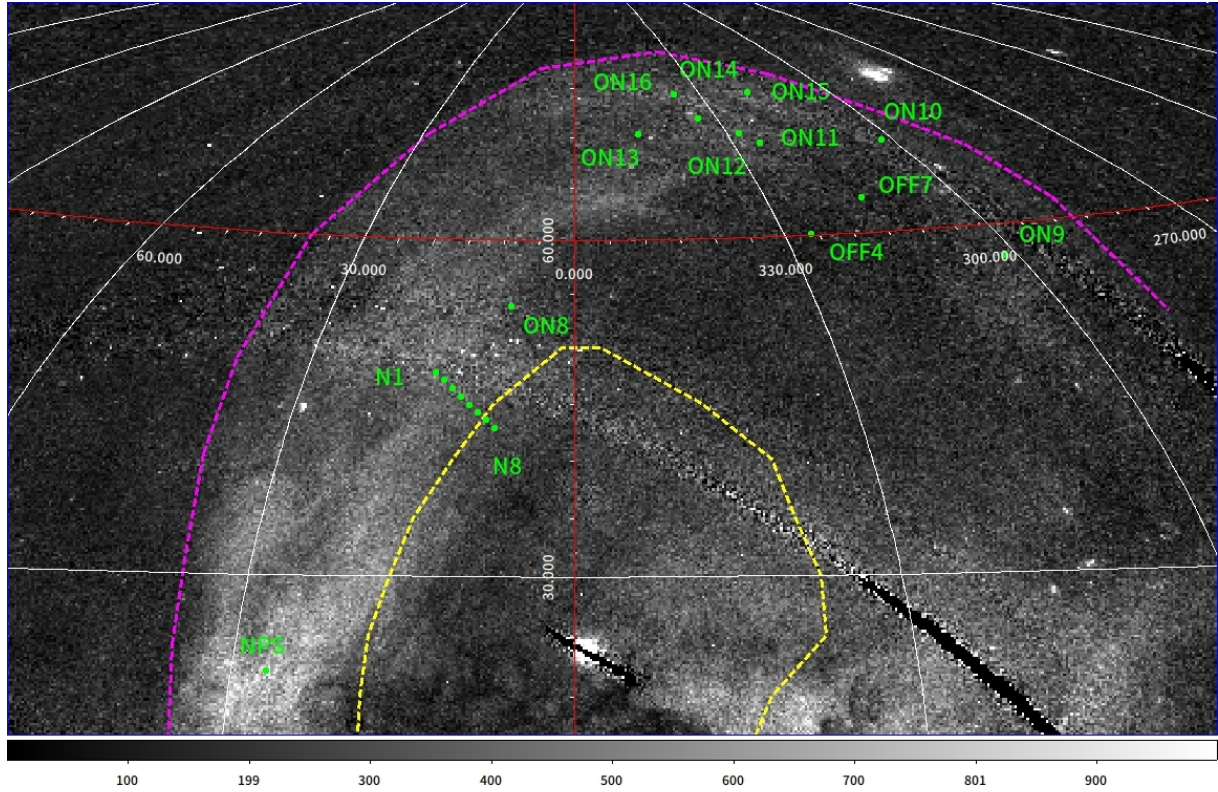[3] https://cxc.harvard.edu/toolkit/colden.jsp

Figure 1. Observation region by *Suzaku* shown on a 0.75 keV image of the *ROSAT*. The region corresponds to the northern part of the Fermi bubbles. This image is displayed on a linear scale, and the color bar at the bottom is 10^6 counts s^{-1}. Numbers written in white are galactic coordinates for longitude and latitude. The green circle corresponds to Suzaku's XIS field of view (17.8 arcmin). The yellow dashed line is the boundary of the bubble proposed in Su et al. (2010), and the magenta dashed line is the NPS/Loop I structure's outer edge (see, Sec.3.2 for more details).
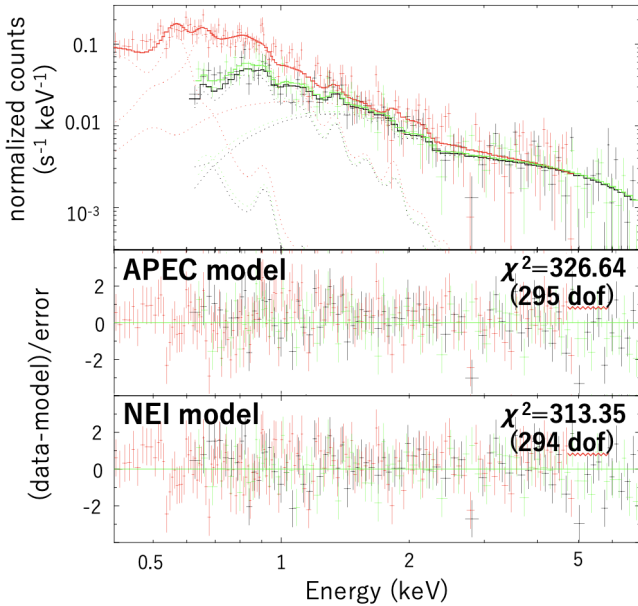

Figure 2. An example of data analysis (in N8 region). XIS spectra of the diffuse emission with the best-fit model curve in the upper column. The XIS0 data/model are shown in black, XIS1 in red, and XIS3 in green. The middle panels show the `apec` model, and the bottom panels show the `nei` model and data residual. See the text for details on fitting the models.

the variation of the EM with the angle from the edge is more obvious in the `nei` model than in the `apec` model.

We find that the electron temperature steeply decreases from 0.5 keV at $\Delta\theta \sim -20°$ to 0.3 keV at $-10°$, and then increases to ~ 0.6 keV towards the outer edge at $\Delta\theta \sim 0°$, where $\Delta\theta$ is the angular distance from the outer edge of Loop I toward inside.

Figure 3 also indicates that regions with plasma closer to the CIE state show larger density-weighted timescale and lower temperature. This means that when the electron density is high, the density-weighted timescale will also be large because n_e is large if the shock age is comparable. In the brightest spot of the NPS, $n_e t \simeq 1.5 \times 10^{11}$ s cm^{-3}; thus, it has not yet reached the CIE state. For the high-latitude NPS/Loop I region, there is no significant position dependence, but assuming the `nei` model, the plasma is in the overall NEI state and the temperature of the plasma is approximately $kT \simeq 0.6$keV.

Note that, the EM and electron temperature kT of the GH component of the NPS/Loop I plasma have a good negative correlation under the assumption of the `nei` model. This correlation between the EM and electron temperature is shown in Fig.4. The correlation coefficient between the EM and plasma temperature is -0.858 assuming the NEI state, which is significantly larger than the negative correlation of -0.484 obtained from when assuming the CIE state.

3.3 F-test

According to Table 2, the `nei` model provides better fitting results than `apec` in most regions, although the results of `apec` are acceptable in terms of the values of the reduced chi-square (χ^2/dof). To

Table 2. Results of fitted parameters of diffuse emission of GH in NPS/Loop I

Name	apec model (CIE)			nei model (NEI)				F−test
	kT_{GH} [a] (keV)	EM_{GH} [b] (10^{-2}cm^{-6}pc)	χ^2/dof	kT_{GH} [c] (keV)	EM_{GH} [d] (10^{-2}cm^{-6}pc)	$n_e t_{GH}$ [e] (10^{11}s/cm^{-3})	χ^2/dof	P−value [f]
			low-latitude NPS/Loop I region ($b < 50°$)					
N1	$0.307^{+0.011}_{-0.010}$	$5.31^{+0.37}_{-0.35}$	293.45/280	$0.307^{+0.023}_{-0.010}$	$5.27^{+0.32}_{-0.80}$	> 4.40	291.36/279	1.58×10^{-1}
N2	$0.315^{+0.014}_{-0.012}$	$5.27^{+0.39}_{-0.39}$	297.78/259	$0.373^{+0.050}_{-0.050}$	$3.66^{+1.29}_{-0.76}$	$3.86^{+5.20}_{-1.51}$	294.11/258	7.39×10^{-2}
N3	$0.311^{+0.012}_{-0.011}$	$5.61^{+0.40}_{-0.37}$	282.59/297	$0.395^{+0.046}_{-0.045}$	$3.38^{+0.88}_{-0.59}$	$2.90^{+2.12}_{-0.96}$	278.05/296	2.87×10^{-2}
N4	$0.303^{+0.010}_{-0.009}$	$5.76^{+0.37}_{-0.39}$	344.16/300	$0.442^{+0.034}_{-0.056}$	$2.69^{+0.76}_{-0.29}$	$1.85^{+1.22}_{-0.42}$	336.78/299	1.10×10^{-2}
N5	$0.277^{+0.010}_{-0.010}$	$5.65^{+0.46}_{-0.42}$	285.00/271	$0.508^{+0.052}_{-0.042}$	$1.71^{+0.0.25}_{-0.23}$	$0.90^{+0.34}_{-0.25}$	269.05/270	8.16×10^{-5}
N6	$0.298^{+0.014}_{-0.012}$	$3.85^{+0.34}_{-0.33}$	290.45/274	$0.505^{+0.060}_{-0.058}$	$1.44^{+0.29}_{-0.22}$	$1.21^{+0.57}_{-0.37}$	285.01/273	2.32×10^{-2}
N7	$0.274^{+0.011}_{-0.011}$	$5.00^{+0.48}_{-0.39}$	274.49/249	$0.556^{+0.161}_{-0.058}$	$1.27^{+0.25}_{-0.32}$	$0.60^{+0.33}_{-0.38}$	264.21/248	8.80×10^{-3}
N8	$0.268^{+0.010}_{-0.009}$	$4.69^{+0.40}_{-0.38}$	326.64/295	$0.605^{+0.115}_{-0.074}$	$1.05^{+0.17}_{-0.18}$	$0.49^{+0.23}_{-0.21}$	313.35/294	4.80×10^{-4}
NPS	$0.291^{+0.003}_{-0.003}$	$15.2^{+0.29}_{-0.29}$	958.22/654	$0.459^{+0.010}_{-0.008}$	$6.26^{+0.26}_{-0.14}$	$1.53^{+0.13}_{-0.10}$	914.41/653	3.28×10^{-8}
			high-latitude NPS/Loop I region ($b > 50°$)					
ON-8	$0.320^{+0.013}_{-0.011}$	$2.98^{+0.19}_{-0.20}$	454.20/417	$0.415^{+0.038}_{-0.053}$	$1.80^{+0.50}_{-0.24}$	$2.74^{+2.02}_{-0.66}$	448.29/416	1.97×10^{-2}
ON-9	$0.282^{+0.010}_{-0.008}$	$3.67^{+0.25}_{-0.25}$	447.44/455	$0.536^{+0.047}_{-0.047}$	$1.10^{+0.17}_{-0.12}$	$0.84^{+0.31}_{-0.21}$	431.28/454	4.42×10^{-5}
ON-10	$0.272^{+0.010}_{-0.010}$	$2.50^{+0.21}_{-0.19}$	447.66/407	$0.658^{+0.497}_{-0.085}$	$0.58^{+0.11}_{-0.20}$	$0.52^{+0.26}_{-0.39}$	428.58/406	2.64×10^{-5}
ON-11	$0.342^{+0.027}_{-0.020}$	$2.65^{+0.28}_{-0.29}$	247.95/148	$0.547^{+0.046}_{-0.031}$	$1.27^{+0.14}_{-0.13}$	$1.43^{+0.26}_{-0.33}$	233.29/147	2.81×10^{-3}
ON-12	$0.347^{+0.026}_{-0.021}$	$2.92^{+0.31}_{-0.30}$	233.7/224	$0.577^{+0.042}_{-0.017}$	$1.35^{+0.11}_{-0.12}$	$1.20^{+0.17}_{-0.24}$	201.82/223	1.11×10^{-8}
ON-13	$0.340^{+0.017}_{-0.013}$	$2.37^{+0.16}_{-0.18}$	498.43/445	$0.499^{+0.033}_{-0.028}$	$1.28^{+0.12}_{-0.11}$	$1.86^{+0.39}_{-0.32}$	477.34/444	1.19×10^{-5}
ON-14	$0.327^{+0.012}_{-0.012}$	$3.03^{+0.21}_{-0.18}$	664.23/568	$0.537^{+0.027}_{-0.025}$	$1.33^{+0.10}_{-0.09}$	$1.33^{+0.21}_{-0.18}$	403.5/567	2.27×10^{-63}
ON-15	$0.259^{+0.006}_{-0.006}$	$5.34^{+0.31}_{-0.27}$	394.93/360	$0.459^{+0.057}_{-0.033}$	$1.43^{+0.16}_{-0.20}$	$0.45^{+0.20}_{-0.14}$	403.5/359	-
ON-16	$0.256^{+0.012}_{-0.012}$	$4.47^{+0.56}_{-0.45}$	188.18/179	$0.540^{+0.121}_{-0.095}$	$1.00^{+0.31}_{-0.18}$	$0.53^{+0.43}_{-0.21}$	185.91/178	1.42×10^{-1}
OFF-4	$0.396^{+0.208}_{-0.075}$	$0.68^{+0.25}_{-0.25}$	153.15/154	$0.582^{+0.146}_{-0.138}$	$0.39^{+0.17}_{-0.10}$	$1.52^{+2.45}_{-0.82}$	150.44/153	9.89×10^{-2}
OFF-7	$0.252^{+0.020}_{-0.017}$	$2.00^{+0.40}_{-0.32}$	201.88/216	$0.748^{+17.420}_{-0.217}$	$0.33^{+0.13}_{-0.11}$	$0.29^{+0.39}_{-0.25}$	197.05/215	2.27×10^{-2}

Note - We fixed the metal abundance of the GH in the NPS/Loop I to $Z = 0.2Z_\odot$. The absorption column densities for the GH in the NPS/Loop I and CXB components were fixed to the Galactic values given by Dickey & Lockman (1990).
[a] Temperature of thermal plasma of the GH under the assumption of CIE (apec model) in NPS/Loop I.
[b] Emission measure of thermal plasma of the GH under the assumption of CIE (apec model) in NPS/Loop I.
[c] Temperature of thermal plasma of the GH under the assumption of NEI (nei model) in NPS/Loop I.
[d] Emission measure of thermal plasma of the GH under the assumption of NEI (nei model) in NPS/Loop I.
[e] Density-weighted timescale of thermal plasma of the GH under the assumption of NEI (nei model) in NPS/Loop I. It reaches ionization equilibrium at approximately $n_e t \simeq 10^{12}$. [f] The probability that the chi-square distributions of the apec and nei models coincide, estimated using the F-test.

evaluate the validity of introducing the nei model, we conducted an F-test. The F-test compares two chi-square distributions and examines the relationship between them under the null hypothesis that the two distributions are equally distributed. If the null hypothesis is correct, then F_χ

$$F_\chi = \frac{\chi_1^2/\nu_1}{\chi_2^2/\nu_2} \qquad (1)$$

follows an F distribution, where χ_1^2, χ_2^2 are the chi-square of the apec and nei models with degrees of freedom ν_1 and ν_2. The smaller F_χ is, the more consistent the two chi-square distributions are, and the probability that the models are consistent is expressed by

$$P_F(F; \nu_1, \nu_2) = \int_F^\infty p_f(f; \nu_1, \nu_2)df \qquad (2)$$

where $p_f(f; \nu_1, \nu_2)$ is the probability density function expressed using the Γ function (Bevington & Robinson 2003). The p-values for the application of the apec and nei models in the analysis are shown in Table 2. In most regions, the P-value is below 0.05, so the null hypothesis is rejected considering a 95% confidence interval and statistical significance between two models is guaranteed.

It is, however, noted that the apec model is also able to reproduce the spectrum effectively, so CIE cannot be completely rejected from statistical perspective. Since the apec model represents the CIE, we

can say that the density-weighted parameter in the apec model is $n_e t \sim 10^{12-13}$ s cm^{-3} or higher. Therefore, the nei contains another free parameter, which is density-weighted parameter, when fitting the data, thus reduced chi-squared values tend to be smaller than corresponding apec model.

For example, the plasma in N1, which is the farthest region from the GC in the low-latitude NPS (see, Fig. 1), has almost reached the CIE, so the density-weighted timescale $n_e t$ in fitting assuming the NEI can only give a lower limit. Thus, if the plasma has reached ionization equilibrium, the apec and nei models lead to the same spectrum. In fact, in the N1 region, the fitting results of the apec and nei models are consistent within the error (see, Table 3). This result indicates that the NEI includes the CIE, which is physically natural.

4 DISCUSSION AND CONCLUSION

4.1 Corroboration of explosion in GC

Table 2 shows that the density-weighted timescale $n_e t$ of NPS/Loop I is of the order of $n_e t \simeq 10^{11}$ s cm^{-3}, which indicates that the plasma is close to CIE, but still in the state of NEI. On the other hand, the electron density n_e of the plasma is estimated to be as small as $n_e \sim 3 \times 10^{-3}$ cm^{-3} (Kataoka et al. 2015). In our case, the measured range of n_e was in the range of $(2-5) \times 10^{-3}$ cm^{-3} assuming
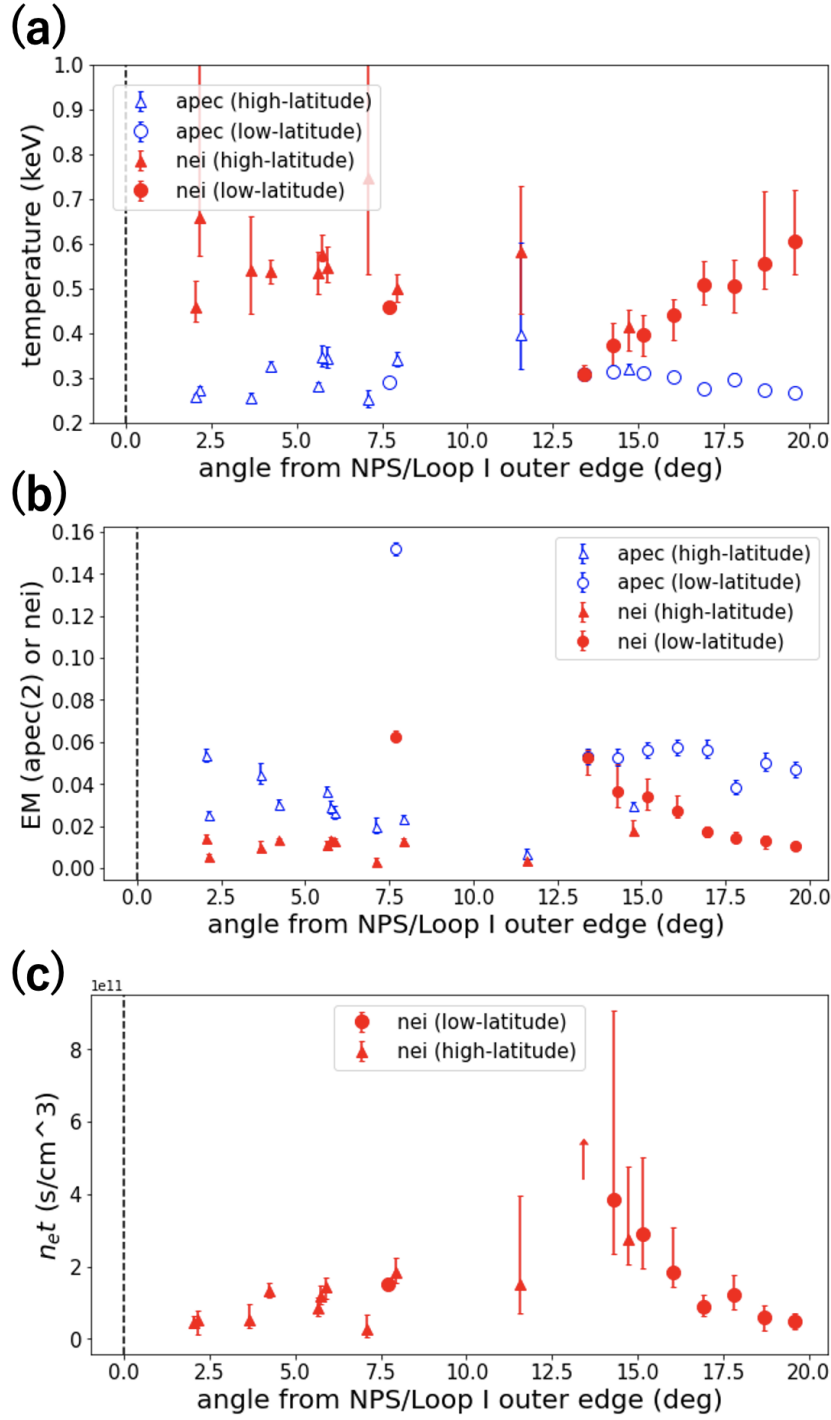
(a)

(b)

(c)

Figure 3. Comparison of fitting results of the GH components in the NPS/Loop I region using `apec` and `nei` models. These are plotted against the angular distance from the inner edge of the NPS/Loop I defined in Table 3 and Fig.1 represented by magenta dashed line.

(a) Electron temperature, kT. (b) Emission measure (EM). (c) Density-weighted timescale $n_e t$.

the scale length of the structure is 2 kpc (see Eq.(1) in Stawarz et al. (2013) for the conversion of EM to electron number density n_e), and thus is consistent with Kataoka et al. (2015). The electron density in each region is calculated on the assumption that the explosion occurs near the GC, as shown in Fig.5. Also, the energy of the explosion can be estimated as $E \simeq n_g \times kT \times V \sim 10^{54-55}$ erg, where $n_g \simeq n_e$ is

the gas number density, and V is the total volume of the compressed NPS/Loop I gas.

In this paper, we assumed that the absorbed hot thermal plasma exists in the NPS and is regarded as a single component; however, there are also other studies in which the absorbed $kT \sim 0.1$ keV thermal plasma exists in addition to $kT \sim 0.3$ keV plasma (Miller et al. 2008; LaRocca et al. 2020). They also consider the absorbed
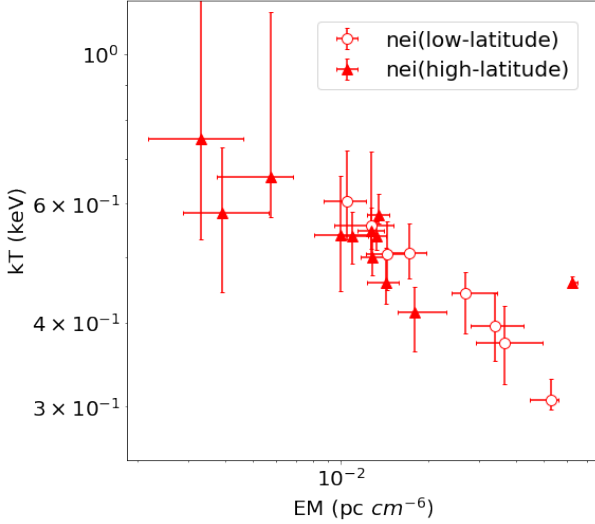
Figure 4. Correlation between EM and temperature kT for GH plasmas in NPS/Loop I under the assumption of NEI state. In this figure, the *circles* represents low-latitude, the *filled triangles* represent high-latitude.

Table 3. Definition of the outer coordinates of the NPS/Loop I arc.

$(l, b$ [deg])
(33.1, 9.9)
(34.5, 16.2)
(35.5, 24.0)
(36.3, 31.7)
(37.6, 40.1)
(38.4, 48.6)
(37.6, 59.9)
(28.9, 70.0)
(9.6, 77.0)
(333.4, 78.5)
(308.6, 75.6)
(295.4, 71.0)
(288.5, 67.2)
(286.3, 61.8)
(287.6, 51.3)

Note - l is Galactic longitude, and b is Galactic latitude in Galactic coordinate.

thermal plasma of $kT \sim 0.1$ keV to be a cool component of the NPS. In fact, the EM of the unabsorbed $kT \sim 0.1$ keV thermal plasma, which we consider to be the LHB/SWCX component in our analysis, is significantly larger than the average EM of the LHB before excluding the SWCX contribution (Snowden et al. 2014). However, the details of the origin and the amount of absorption of $kT \sim 0.1$ keV are still under debate.

For example, Henley & Shelton (2015) analyzed a large set of *XMM-Newton* and *Suzaku* shadowing observations to discriminate the relative contributions of LHB and SWCX and discussed the possible uncertainties in the estimated temperature and brightness of the Galactic halo. These satellites carry CCD cameras with high spectral resolutions, allowing important line emission features to determine the plasma temperature (e.g., O VII and O VIII) to be resolved. Unfortunately, these CCD cameras are only usable above ~0.4 keV energy band; thus, it is difficult to determine the spectral properties of $kT \simeq 0.1$ keV plasma. Similarly, Liu et al. (2017) re-

visited the RASS data to produce the "cleaned" maps of only the LHB. They incorporated the most recent observations from a sound rocket mission, *DXL*, to quantify and characterize the contribution of SWCX to RASS data as measured in the 1/4 keV band. However, an accurate estimation of the SWCX is still difficult, owing to low-spectral-resolution proportional counters on board *ROSAT*. Moreover, the contribution of SWCX varies largely both in the time and space. They concluded that the total energy enclosed in the LHB may be more than 15 times smaller that estimated without removing the SWCX contribution. Together with an unknown amount of absorption as described above, an accurate measurement of the LHB is yet far from being complete and requires further clarifications.

Thus, we attempted to fit the data by assuming another extreme case, in which $kT \sim 0.1$ keV plasma is fully absorbed with $N_H = N_{Gal}$; however, the results were unchanged for all the other remaining parameters, namely, normalization, the temperature of $kT \sim 0.3$ keV plasma, and the normalization of the CXB, within a one sigma statistical uncertainty. These results suggested that the absorbed thermal plasma of the NPS was in the NEI state, irrespective of the origin or amount of interstellar absorption of the plasma at $kT \sim 0.1$ keV. Also, if there exists an absorbed thermal plasma of $kT \sim 0.1$ keV exist in the NPS, as suggested by LaRocca et al. (2020), this cool component may dominate the total energy stored in the NPS, which further supports our hypothesis that the NPS is created by a huge past explosion of the GC.

Importantly, such a large density-weighted timescale $n_e t$ with such a low electron number density n_e requires a large shock age t. In fact, assuming the nei model, the shock age is calculated from the EM and density-weighted timescale to be around $t \sim$ Myr.

Fig.5 shows the calculation of the shock age t based on the electron density n_e and density-weighted timescale $n_e t$ in each region. This time can be interpreted as the elapsed time after the shock front arrived and heated the plasma in the corresponding position of the GH. Therefore, this time must be shorter than the age of the present shock front forming the NPS. This is consistent with the estimated age of the bubble produced by a nuclear outburst occurred in the GC about 10 Myr ago (Sofue 1977, 2000).

Conversely, if the NPS/Loop I structures are associated with a nearby SNR, these structures may be located approximately ~100 pc apart from the Sun. Even in such a case, we can calculate the electron density and shock age in the same way, but we obtain $n_e \simeq 2 \times 10^{-2}$cm^{-3} for the electron density assuming the depth of the gas is 50 pc, and $t \simeq 300$ kyr for the shock age. Thus, the plasma density is much lower than the typical ISM density of $n_e \sim 1$cm^{-3}. For example, a shell of the Cygnus loop, which is an SNR located at the distance of 540 pc from the sun, has an electron density of $n_e \simeq 1.0$ cm^{-3} (Sun et al. 2006), and the shell of the superbubble in the OB association has an electron density of $n_e \simeq 3$ cm^{-3} (Tomisaka & Ikeuchi 1986). Thus, the density of NPS/Loop I is exceptionally thin compared to those of the shell in the SNRs near the solar system. In addition, the shock age of the NPS/Loop I is too long compared to that of typical Galactic SNRs. Furthermore, the energy of the structure, assuming an SNR, is $E \simeq n_g \times kT \times V \sim 10^{52}$erg, which is almost equivalent to the energy emitted by a few dozen typical type-II SNRs, and is thus not plausible. Of course, the energy E can vary largely with the volume V, which depends sensitively on the distance to the structure. However, if the NPS/Loop I was really a nearby SNR close to the sun, it is unusual that the corresponding optical emission, such as bright Hα filaments as seen in Cygnus Loop (Levenson et al. 1998), is hardly seen in the case of NPS/Loop I.
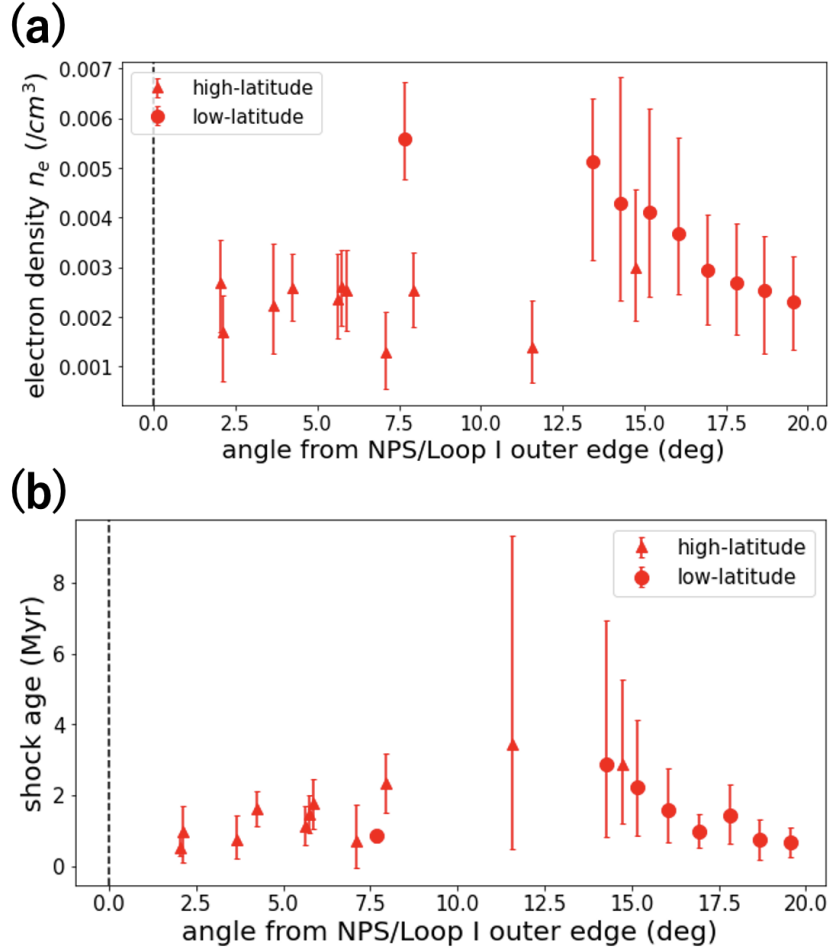
(a)

(b)

Figure 5. Spatial distribution of (a)electron density n_e , and (b)shock age t , assuming that the plasma is in the NEI state and explosion was around the GC. These are plotted against the angular distance from the inner edge of the NPS/Loop I defined in Table 3 and Fig.1 represented by magenta dashed line.

4.2 Plasma State in NPS/Loop I

In this context, the comparison of timescales to reach equilibrium in the X-ray emitting plasma provides additional support for the `nei` state in the NPS/Loop I structure. It is believed that this plasma is swept up by the shock and then heated to emit X-ray. When the plasma is heated by the shock wave, the proton temperature is initially $m_p/m_e \simeq 1836$ times higher than that of electrons, where m_p and m_e are the masses of protons and electrons, respectively. Over time, the kinetic energy of the protons is transferred to the electrons, moving closer to thermal equilibrium. By adopting the equations in Spitzer (1962) normalized to typical values in the NPS/Loop I region, we obtain the relaxation time, which is equal to the time of equipartition, as

$$t_{ep} \sim 1.1 \times 10^6 \left(\frac{n_e}{3 \times 10^{-3} \text{cm}^{-3}} \right)^{-1} \left(\frac{kT_e}{0.3 \text{ keV}} \right)^{3/2} \text{yr} \quad (3)$$

where T_e is the electron temperature. For comparison, the self-collision time due to collisions between protons and electrons in each group is expressed by

$$t_{pp} \sim 2.6 \times 10^5 \left(\frac{n_e}{3 \times 10^{-3} \text{cm}^{-3}} \right)^{-1} \left(\frac{kT_e}{0.3 \text{ keV}} \right)^{3/2} \text{yr} \quad (4)$$

$$t_{ee} \sim 620 \left(\frac{n_e}{3 \times 10^{-3} \text{cm}^{-3}} \right)^{-1} \left(\frac{kT_e}{0.3 \text{ keV}} \right)^{3/2} \text{yr} \quad (5)$$

where t_{pp} is the proton-proton and t_{ee} is the electron-electron self-collision time, and after this time, these particles attain a Maxwell distribution.

On the other hand, instantaneous heating via the shock wave breaks the ionization state from its initial equilibrium state, resulting in the NEI state. In order that such NEI plasma reaches an approximate CIE, $n_e t \simeq 10^{12} \text{ cm}^{-3}\text{s}$ is necessary. Hence a typical timescale for the transition to the CIE state is given by

$$t_{\text{CIE}} \sim 10^7 \left(\frac{n_e}{3 \times 10^{-3} \text{cm}^{-3}} \right)^{-1} \text{yr} \quad (6)$$

.

As calculated in Section 4.1 and Eq. 3, 4, and 5, it can be said that the electron temperature T_e and proton temperature T_p are close to equilibrium, that is, $T_e \sim T_p$ if NPS/Loop I is a Myr-scale event. However, Eq. 6 shows that the ionization state of the plasma, represented by the temperature T_z, does not reach equilibrium, and is most likely in the NEI state. This is consistent with the analysis in Section 3.3, where the CIE represents the overall features of the observed X-ray spectra, while the NEI provides a better representation of data in

terms of the results of reduced chi-squared and F-test. It is important to note that statistically, CIE cannot be completely rejected. If the plasma state is in CIE, the density-weighted timescale is $n_e t \simeq 10^{12}$ s cm^{-3}, and the shock age is close to Eq. 6.

4.3 Time Evolution of the Plasma

Continuous observations of the low-latitude NPS/Loop I region across the bubble edge and analysis assuming the `nei` model show that the electron temperature is cooler, brighter, and closer to the CIE toward the outside of the GC (see, red circle plot in Fig. 3). Such a gradient may be caused by the time evolution of the shock wave. The temperature is lower toward the outer side of the GC because of the slower shock wave, but brighter because a higher amount of ISM has been swept up. Furthermore, these tendency appears to be similar to what was anticipated from the radial profile of the density and temperature described by the self-similar solution under the assumption that the Shock front is mostly outside of the GC. However, further careful simulation or modeling is necessary. HaloSat observations show a similar temperature gradient within the NPS (LaRocca et al. 2020). In addition, the density-weighted timescale gradually increased toward the outer regions of the NPS, reflecting a gradual increase in the plasma density n_e.

It is not clear whether the plasma temperature and the velocity of the shock wave directly connected, but if we consider the high-latitude region close to the outer edge of NPS/Loop I as the shock front, we can roughly estimate the velocity of the shock wave as in Kataoka et al. (2013) assuming the `nei` model. Because a typical GH temperature is 0.2 keV and the speed of sound is approximately $C_s \sim 200 \mathrm{km\,s^{-1}}$, and according to Rankine-Hugoniot equation, the observed electron temperature of the high-latitude NPS/Loop I $kT \sim 0.5-0.6\mathrm{keV}$ corresponds to a shock velocity with a Mach number $M \geq 2.3-2.7$. Hence the velocity of the shock wave in NPS/Loop I is estimated to be $v \geq 460-530$ km s^{-1}. In this context, Miller & Bregman (2016) derived a similar range of the $v = 490^{+230}_{-77}$ km s^{-1} expansion velocity using the O$_{\mathrm{VII}}$ and O$_{\mathrm{VIII}}$ emission lines, although the paper assumed a slightly different model that contains an underlying $kT \simeq 0.2$ keV halo emission that co-exists with the shocked component described above.

Although gradual changes in kT, EM, and $n_e t$ are seen in the continuous observation of low-latitude NPS with distance from the NPS/Loop I inner edge, such a sequential trend does *not* seem to smoothly connect with the parameters in the high-latitude NPS/Loop I, as shown in Fig. 3. Meanwhile, the plasma in the Loop I is also well described by NEI with an density-weighted timescale of about $n_e t \sim 10^{11}\mathrm{s\,cm^{-3}}$ and an electron temperature of $kT \sim 0.5-0.6\mathrm{keV}$, which is significantly higher than typical GH temperatures. This fact may suggest that the NPS/Loop I structure have resulted from multiple explosions. However, the observations in the high-latitude NPS/Loop I are not spatially continuous and sparse, so the cause of the lack of continuity is most likely undersampling.Sensitive all-sky surveys with soft X-rays, such as eROSITA, will provide us with new results to address these problems. Additional systematic surveys are necessary to discuss the past activity of the galaxy in detail.

DATA AVAILABILITY

The data from the XIS detector by *Suzaku* is available from heasarc archieve (https://heasarc.gsfc.nasa.gov/cgi-bin/W3Browse/w3browse.pl). CALDB was used for calibration data, and the HEASOFT suite of tools was used for data analysis.

REFERENCES

Akita M., Kataoka J., Arimoto M., Sofue Y., Totani T., Inoue Y., Nakashima S., 2018, ApJ, 862, 88
Atwood W. B., et al., 2009, ApJ, 697, 1071
Bamba A., Yamazaki R., Ueno M., Koyama K., 2003, ApJ, 589, 827
Berkhuijsen E. M., Haslam C. G. T., Salter C. J., 1971, A&A, 14, 252
Bevington P. R., Robinson D. K., 2003, Data reduction and error analysis for the physical sciences; 3rd ed.. McGraw-Hill, New York, NY, https://cds.cern.ch/record/1305448
Bingham R. G., 1967, MNRAS, 137, 157
Bland-Hawthorn J., Cohen M., 2003, ApJ, 582, 246
Borkowski K. J., Lyerly W. J., Reynolds S. P., 2001, ApJ, 548, 820
Dickey J. M., Lockman F. J., 1990, ARA&A, 28, 215
Egger R. J., Aschenbach B., 1995, A&A, 294, L25
Finkbeiner D. P., 2004, ApJ, 614, 186
Haslam C. G. T., Salter C. J., Stoffel H., Wilson W. E., 1982, A&AS, 47, 1
Henley D. B., Shelton R. L., 2015, ApJ, 808, 22
Ishisaki Y., et al., 2007, PASJ, 59, 113
Kataoka J., et al., 2013, ApJ, 779, 57
Kataoka J., Tahara M., Totani T., Sofue Y., Inoue Y., Nakashima S., Cheung C. C., 2015, ApJ, 807, 77
Kataoka J., Sofue Y., Inoue Y., Akita M., Nakashima S., Totani T., 2018, Galaxies, 6, 27
Kataoka J., Yamamoto M., Nakamura Y., Ito S., Sofue Y., Inoue Y., Nakamori T., Totani T., 2021, ApJ, 908, 14
Kelley R. L., et al., 2007, PASJ, 59, 77
Koyama K., et al., 2007, PASJ, 59, 23
Kushino A., Ishisaki Y., Morita U., Yamasaki N. Y., Ishida M., Ohashi T., Ueda Y., 2002, PASJ, 54, 327
LaRocca D. M., Kaaret P., Kuntz K. D., Hodges-Kluck E., Zajczyk A., Bluem J., Ringuette R., Jahoda K. M., 2020, ApJ, 904, 54
Levenson N. A., Graham J. R., Keller L. D., Richter M. J., 1998, ApJS, 118, 541
Liu W., et al., 2017, ApJ, 834, 33
Miller M. J., Bregman J. N., 2016, ApJ, 829, 9
Miller E. D., et al., 2008, PASJ, 60, S95
Mitsuda K., et al., 2007, PASJ, 59, S1
Panopoulou G. V., Dickinson C., Readhead A. C. S., Pearson T. J., Peel M. W., 2021, arXiv e-prints, p. arXiv:2106.14267
Planck Collaboration et al., 2013, A&A, 554, A139
Predehl P., et al., 2020, Nature, 588, 227
Predehl P., et al., 2021, A&A, 647, A1
Smith R. K., Hughes J. P., 2010, ApJ, 718, 583
Snowden S. L., et al., 1995, ApJ, 454, 643
Snowden S. L., et al., 2014, ApJ, 791, L14
Sofue Y., 1977, A&A, 60, 327
Sofue Y., 2000, ApJ, 540, 224
Sofue Y., 2015, MNRAS, 447, 3824
Sofue Y., Kataoka J., 2021, MNRAS, 506, 2170
Spitzer L., 1962, Physics of Fully Ionized Gases
Stawarz Ł., et al., 2013, ApJ, 766, 48
Su M., Slatyer T. R., Finkbeiner D. P., 2010, ApJ, 724, 1044
Sun X. H., Reich W., Han J. L., Reich P., Wielebinski R., 2006, A&A, 447, 937
Takahashi T., et al., 2007, PASJ, 59, 35
Tawa N., et al., 2008, PASJ, 60, S11
Tomisaka K., Ikeuchi S., 1986, PASJ, 38, 697
Vidal M., Dickinson C., Davies R. D., Leahy J. P., 2015, MNRAS, 452, 656

Willingale R., Bleeker J. A. M., van der Heyden K. J., Kaastra J. S., Vink J.,
     2002, A&A, 381, 1039
Yoshino T., et al., 2009, PASJ, 61, 805

APPENDIX A: DETAILED MODELING OF THE PLASMA WITH $KT \simeq 0.1$ KEV

As discussed in the text (Sections 3.1 and 4.1), we analysed assuming a single unabsorbed $kT \simeq 0.1$ keV plasma to mimic the low-energy X-ray emission from LHB/SWCX. However, certain studies (Miller et al. 2008; LaRocca et al. 2020) have proposed the existence of cool component $kT \simeq 0.1$ keV of NPS, in addition to LHB/SWCX emission. The origin of such cool component is still far from being understood. Thus, in this appendix, we thus tried to fit the same spectra with various emission models, namely (1) double NPS (CIE + CIE), in which both cool ($kT \simeq 0.1$ keV) and hot ($kT \simeq 0.3$ keV) components exist in the NPS and modeled as CIE, (2) double NPS (CIE+NEI), where the same spectrum is modeled as CIE + NEI, and (3) absorbed LHB, where the temperature of the cool component is fixed at $kT \simeq 0.1$ keV but absorbed as the same amount with the NPS. The LHB/SWCX component in (1) and (2) ia absorbed at the galactic value of the neutral absorption column density $N_{\rm H,Gal}$. The example results of spectral fitting for the N8 region in the low-latitude NPS/Loop I region are summarized in Table A4. Note that, irrespective of the amount of absorption assumed, the temperature of the cool component is always converged to $kT \simeq 0.1$ keV and that of the hot component is $kT \simeq 0.6$ keV, respectively. Thus, the results are consistent with that shown in Section 3.1 within $1\,\sigma$ statistical uncertainty. Therefore, we conclude that the discussion and conclusion in this study would not be affected even though the physical origin of $kT \simeq 0.1$ keV cool component remains uncertain.

This paper has been typeset from a TeX/LaTeX file prepared by the author.

Table A4. Results of fitted parameters of diffuse emission of GH in NPS/Loop I in N8

number	model	LHB	NPS(cool component)		NPS(hot component)			χ^2/dof
		EM $(10^{-2}\mathrm{cm}^{-6}\mathrm{pc})$	kT (keV)	EM $(10^{-2}\mathrm{cm}^{-6}\mathrm{pc})$	kT (keV)	$n_e t_{GH}$ $(10^{11}\mathrm{s/cm}^{-3})$	EM $(10^{-2}\mathrm{cm}^{-6}\mathrm{pc})$	
(1)	double NPS (CIE+CIE) [a]	< 3.18	$0.092^{+0.001}_{-0.007}$	$28.1^{+22.1}_{-21.9}$	$0.268^{+0.011}_{-0.010}$	$-$	$4.33^{4.24}_{-4.09}$	325.37/293
(2)	double NPS (CIE+NEI) [b]	< 1.56	$0.081^{+0.013}_{-0.023}$	$74.4^{+51.1}_{-34.9}$	$0.661^{+0.132}_{-0.116}$	$3.05^{+3.01}_{-1.23}$	$0.94^{0.22}_{-0.13}$	307.64/292
(3)	absorbed LHB [c]	$5.75^{+0.55}_{-0.72}$	$-$	$-$	$0.608^{+0.115}_{-0.067}$	$5.43^{+2.32}_{-2.22}$	$0.981^{+0.146}_{-0.170}$	312.94/294

Note - We fixed the metal abundance of the GH in the NPS/Loop I to $Z = 0.2Z_\odot$. The absorption column densities for the GH in the NPS/Loop I and CXB components were fixed to the Galactic values given by Dickey & Lockman (1990).

[a] `apec + wabs*(apec + apec + powerlaw)`

[b] `apec + wabs*(apec + nei + powerlaw)`

[c] `wabs*(apec + apec + powerlaw)`